Heat Transfer Distributions Around Nominal Ice Accretion Shapes Formed on a Cylinder in the NASA Lewis Icing Research Tunnel

G. J. Van Fossen, R. J. Simoneau,
W. A. Olsen, Jr., and K. J. Shaw
Lewis Research Center
Cleveland, Ohio

NASA

E-1905

HEAT TRANSFER DISTRIBUTIONS AROUND NOMINAL ICE ACCRETION SHAPES FORMED ON A CYLINDER IN THE NASA LEWIS ICING RESEARCH TUNNEL

G. J. Van Fossen, R. J. Simoneau, W. A. Olsen, and R. J. Shaw

National Aeronautics and Space Administration
Lewis Research Center
Cleveland, Ohio 44135

Abstract

Local heat transfer coefficients were obtained on irregular cylindrical shapes which typify the accretion of ice on circular cylinders in cross flow. The ice shapes were grown on a 5.1 cm (2.0 in.) diameter cylinder in the NASA Lewis Icing Research Tunnel. The shapes were 2, 5, and 15 min accumulations of glaze ice and 15 min accumulation of rime ice. These icing shapes were averaged axially to obtain a nominal shape of constant cross section for the heat transfer tests. Heat transfer coefficients were also measured around the cylinder with no ice accretion. The models were run in a 15.2 x 68.6 cm (6 x 27 in.) wind tunnel at several velocities. Background turbulence in the wind tunnel was less than 0.5 percent. The models were also run with a turbulence producing grid which gave about 3.5 percent turbulence. The effect of roughness was also simulated with sand grains glued to the surface.

Results are presented as Nusselt number versus angle from the stagnation line for the smooth and rough models for both high and low levels of free stream turbulence. Roughness of the surface in the region prior to flow separation plays a major role in determining the heat transfer distribution. Free stream turbulence does not affect the distribution of heat transfer in this region but raises the level by a nearly uniform amount. For the rime shape, roughness had a larger effect in the near wedge shaped region past the initial separation point.

Nomenclature

a	surface area of heat flow gage, cm^2
A	constant in power law curve fit, Eq. (14)
b	half width of insulation gap between copper heat flow gages, cm
B	constant, power of Reynolds number in Eq. (14)
C	flow parameter defined by Eq. (8)
d	diameter of cylinder, cm
E	voltage, V
g_c	gravitational constant
h	heat transfer coefficient, W/m^2-°C
I	current, amp
k	thermal conductivity, J/m-sec-K
L	length of heat flux gage, cm
Nu	Nusselt number
p	pressure, N/m^2
Pr	Prandtl number
Q	heat flow, W
R	gas constant, J/kg-°C
Re	Reynolds number
r	recovery factor or radial distance, cm
T	temperature, K
Tu	turbulence intensity, percent
V	velocity, m/sec
7	heat flux gage depth under model surface, cm
γ	ratio of specific heats for air
ε	surface emissivity of heat flux gage
σ	Stefan-Boltzman constant, W/m^2-K^4
μ	viscosity, N-sec/m^2
ρ	density, kg/m^3

Subscripts

a	ambient surroundings
ad	adiabatic wall temperature
gap	in the space between copper heat flux gages
i	iteration index
r	at reference conditions
rad	radiation
s	static conditions
t	total conditions
w	wall (copper strip)

Introduction

A portion of the NASA Icing Research Program involves development of computer codes that predict the accretion of ice on surfaces. Experiments show that the ice shape changes drastically in shape and roughness for different conditions.[1,2] Existing codes show that the predicted ice shapes are very sensitive to the assumed heat transfer coefficient distribution.[3] Unfortunately no data for heat transfer coefficients over smooth or rough ice shapes exists in the literature.

In an effort to correct this deficiency, heat transfer coefficient distributions were measured on simulated ice accretion shapes. A range of ice shapes were obtained on a circular cylinder in the NASA Lewis Icing Research Tunnel (IRT). These shapes were axially averaged to obtain a representative ice shape with constant cross-section. Heat transfer models of these axially averaged shapes were then cast from polyurethane foam. Electrically heated copper strips embedded in the model surface were used to measure the heat transfer coefficient distributions around the circumference of each model. Heat transfer distributions were measured in dry air over a range of velocities with these models. Sand was later added to the surface of the models to determine the effect of roughness. The effect of free stream turbulence was also investigated.

Results are presented as Nusselt number versus angle from the stagnation line for the smooth and rough models for both high and low levels of free stream turbulence. The effect of Reynolds number on Nusselt number is also presented for selected locations on each model. A table of curve fits of Nusselt number as a function of Reynolds number for each heat transfer gage is also presented.

Test Specimens

Heat transfer coefficient distributions were measured around models of four ice accretion shapes. The ice shapes were grown on a 5.1 cm (2.0 in.) diameter circular cylinder in the NASA Lewis Icing Research Tunnel (IRT). The shapes were 2-, 5-, and 15-min accumulations of glaze ice and 15-min accumulation of rime ice. These icing shapes were averaged axially to obtain a nominal

shape of constant cross section for the heat transfer tests. This was accomplished by allowing the ice to accrue for the required time on the 5.1 cm (2.0 in) cylinder. Figure 1 shows both glaze and rime ice that accrued on a cylinder in the IRT under similar conditions. The ice was then cut perpendicular to the axis of the cylinder at the tunnel centerline and at locations ±5.1 cm (2.0 in.) from the centerline. Tracings of these cross-sections were then superimposed and an average curve was drawn through them. The four icing shape heat transfer models are shown in Fig. 2. The dimensionless coordinates, as defined on Fig. 3, for each ice shape are given in Table I.

Each model was 15.2 cm (6.0 in.) long. A 5.1 cm (2.0 in.) circular semi-cylinder was attached to the rear of each model shown in Fig. 2 during testing to assure geometric similarity with the ice shapes grown in the IRT.

The icing shape heat transfer models were cast of a polyurethane foam. Axially averaged transfer coefficients were measured around the circumference of each model by using electrically heated copper strips. Each strip was 6.6 cm (2.6 in.) long by 0.51 cm (0.20 in.) wide and 0.318 cm (0.125 in.) deep. A typical copper strip heat flux gage is shown in Fig. 4. A Kapton encapsulated electric heater was fastened to each copper strip with a pressure sensitive adhesive. A stainless steel sheathed, closed, grounded ball, Chromel-Alumel thermocouple was soft soldered into a groove in each copper strip.

The copper strips were embedded in the polyurethane foam at closely spaced intervals along the circumference of each model. The location of the gages for each icing model is shown in Table II. The surface of each model had a thin coating of clear lacquer to keep the copper gages from oxidizing and changing emissivity. As will be shown later, the increased thermal resistance of the lacquer coating did not adversely affect the results.

A large copper plate with a heater and thermocouple similar to the surface gages was embedded in the center of each model to act as guard heater. The temperature of the guard plate was adjusted to be the same as that of the heat flux gages thus minimizing heat loss thru the rear of the model.

Heat transfer coefficients were also measured around the cylinder with no ice accretion. The circular cylinder model was made of wood instead of the polyurethane foam. The cylinder heat transfer model is shown in Fig. 5. The circular cylinder model was 6.6 cm (2.6 in.) in diameter and 15.2 cm (6.0 in.) long. The same copper strip heat flux gages were used in the cylinder as in the icing shape models. A rear guard heater was also used on this model. In addition to the rear guard heater, guard heaters were added at the ends of the heat flux gages because the wood used had a higher thermal conductivity than the polyurethane foam.

In order to more closely simulate the small scale surface roughness of ice, artificial roughness was added to the models for some of the tests. This was accomplished by spraying a coat of clear lacquer onto the model, sand was then sprinkled on the wet surface from an ordinary salt shaker. Another thin coat of lacquer then held the sand in place. A profilometer was used to try and measure the roughness but the roughness elements were too large for this instrument. An optical comparitor was used to obtain an estimate of the roughness. The maximum height of any one roughness element

was found to be 0.0572 cm (0.0225 in.). The average height of the roughness elements above the surface was 0.033 cm (0.013 in.).

Apparatus

The icing shape heat transfer tests were conducted in the wind tunnel shown schematically in Fig. 6. Room air first flowed through a turbulence damping screen with an 18x18 mesh of 0.24 mm (0.0095 in.) diameter wire. Large scale turbulence from the room was then broken up by flowing thru approximately 12 000 plastic soda straws which were 0.64 cm (0.25 in.) in diameter by 19.69 cm (7.75 in.) long. The air then passed through a final damping screen identical to the first.

A 4.85:1 contraction then accelerated the air entering the test section. The maximum velocity attainable in the test section was about 46 m/sec (150 ft/sec, 102 mph) and the clear tunnel turbulence level was less than 0.5 percent at all flow rates. For the high turbulence cases, a turbulence generating biplane grid of 0.318 cm (0.125 in.) rods spaced 6 rod diameters apart was installed 90 rod diameters (28.58 cm (11.25 in.)) upstream of the model leading edge.

The test section was 15.2 cm (6.0 in.) wide by 68.6 cm (27.0 in.) high. The models were mounted horizontally in the tunnel. Hot wire surveys indicated that the center 7.6 cm (3.0 in.) of the tunnel was free from turbulence generated by the sidewalls. The heat flux gages were 6.6 cm (2.6 in.) long and thus did not extend into the region of turbulence generated by the sidewalls.

After leaving the test section, the flow passed through a transition section into a 10 in. pipe, through two long radius elbows, a flow straightener and into an orifice run. The orifice plate had a diameter of 19.1 cm (7.5 in.). The flow rates used in these tests were measured with this orifice. Air then passed thru a 10 in. butterfly valve which was used to control the flow rate and then to the building altitude exhaust system.

The temperature of the air entering the wind tunnel was measured by four exposed ball Chromel-Alumel thermocouples around the perimeter of the inlet. The output of these four thermocouples were averaged to give the total or stagnation temperature.

Turbulence measurements were made with a DISA model 55M10 constant temperature hot wire anemometer. Signals were linearized with a DISA model 55M25 linearizer. The mean component of the turbulent velocity signal was read on a DISA model 55D31 integrating digital voltmeter. The fluctuating component was read on a DISA model 55D35 RMS voltmeter. Both these instruments have an adjustable time constant which was adjusted to the minimum value which would give a stable reading. The hot wire probe was a Thermosystems Inc. model 1227-T1.5. This is a 4×10^{-6} meter tungsten single wire probe. The hot wire was calibrated before each use in a free jet of air at nearly the same temperature (±1° C) as the wind tunnel flow. The hotwire system frequency response was determined to be around 30 kHz by the standard square wave test. All hot wire measurements were made without the models in place and at the location of the cylinder center line.

Turbulence scale was estimated using an autocorrelation of the hot wire signal. The autocorrelation was obtained on a Nicolet model 660A dual channel spectrum analyzer. The area

2

under the autocorrelation function gave an integral time scale. This time scale was then multiplied by the mean velocity to obtain a measure of the integral length scale.

During each heat transfer test, power to each heat flux gage was adjusted to keep the surface of the model at constant temperature. This was done manually at first and required about one hour to attain equilibrium for each data point. An electronic circuit was designed to accomplish this task and the time to set each data point fell to about 5 min. A block diagram of the circuit is shown in Fig. 7. The voltage from the thermocouple was amplified and compared to an adjustable reference voltage which was the same for all heaters on the model. The difference in these two voltages was amplified and applied to the base of a power transistor which then controlled the power to each heater. Current was measured with the 0.05 ohm shunt and voltage was measured across each heater thus allowing the calculation of electric power dissipated.

Data Reduction

Heat Transfer Coefficient

The heat transfer coefficient for each copper strip was calculated from the voltage, and current applied to the heater and the temperature measured by the thermocouple. It was desired to know the heat transfer due only to convection; therefore, the heat lost by radiation had to be subtracted from the electric power input. This contribution was estimated as

$$Q_{rad} = \sigma a \epsilon \left(T_w^4 - T_a^4 \right) \tag{1}$$

The surface emissivity, ϵ, was estimated as 0.5. The radiation contribution for most cases was less than 2 percent of the total heat flow.

The copper strips were separated by a small gap which contained the polyurethane foam. Some heat is conducted from the edge of the copper strip, through the foam and convected from the surface of the model. An estimate of this heat loss was obtained from an exact solution[4] for the heat conduction in a rectangle with two adjacent sides insulated, one other side held at constant temperature (the temperature of the copper strip) and the final side convecting to a fluid at a known temperature. The solution is

$$Q_{gap} = 2h(T_w - T_{ad}) L \sum_{n=1}^{\infty} \frac{\tan \alpha_n Z \tanh \alpha_n b}{\left[\alpha_n^2 + \left(\frac{h}{k} \right)^2 \right] Z + \frac{h}{k}} \tag{2}$$

where the α_n's are the roots of

$$\alpha_n \tan (\alpha_n Z) = \frac{h}{k} \tag{3}$$

A drawing of this area is shown in Fig. 8. A detailed finite difference model of the area between the dashed lines in the figure showed that virtually no heat was lost from the bottom side of the copper strip. The finite difference solution and the exact solution gave the same value for the heat lost in the gap to within 2 percent. The exact solution was used in the data reduction to account for the heat loss thru the gap. The heat lost thru the gap varied from 10 percent to as much as 20 percent for large gaps.

The heat transfer coefficient was then calculated as

$$h = \frac{EI - Q_{rad} - Q_{gap}}{a(T_w - T_{ad})} \tag{4}$$

Note that to calculate Q_{gap}, the heat transfer coefficient, h, must be known. Thus an iterative solution was necessary. An initial guess was made for h from Eq. (4) by assuming Q_{gap} was zero, Q_{gap} was then calculated and Eq. (4) used to recalculate h. This procedure was repeated until

$$\left| h_{i+1} - h_i \right| < 0.001 \tag{5}$$

Test Section Density-Velocity Product

With no models present, the velocity in the test section was measured with a pitot-static probe. The density was calculated assuming air to be an ideal gas. The density-velocity product in the test section was then correlated to the orifice flow rate. This correlation was then used to calculate the density-velocity product in all subsequent tests.

Test Section Static Pressure

Test section static pressure was not measured so an estimate was made using Bernoulli's equation for incompressible flow. Test section static pressure was calculated as

$$P_s = P_t - \frac{1}{2} \rho V^2 \tag{6}$$

The total pressure, P_t, was assumed to be the local barometric pressure. The density-velocity product was known from the correlation mentioned in the previous section. To calculate the density, the static pressure must be known; thus, iteration was required to obtain a solution to Eq. (6).

Test Section Static Temperature

Total temperature was measured at the inlet to the turbulence control section. Test section static temperature was calculated for a perfect gas under adiabatic conditions as

$$T_s = \frac{-1 + \sqrt{1 + \frac{4CT_t}{P_s^2}}}{\frac{2C}{P_s^2}} \tag{7}$$

where

$$C = \frac{\gamma - 1}{2} (\rho V)^2 \frac{R}{\gamma g_c} \tag{8}$$

The ratio of specific heats for air, γ, was assumed to be 1.4 and the gas constant, R, was 286.91 J/kg-°C (53.35 ft-lbf/lbm-°R).

Adiabatic Wall Temperature

The adiabatic wall temperature was calculated as

$$T_{ad} = T_s + r(T_t - T_s) \tag{9}$$

3

The recovery factor, r, was assumed to be

$$r = \sqrt{Pr} \qquad (10)$$

Thermal Properties

Thermal conductivity, viscosity, and Prandtl number for air were obtained as a function of temperature from curve fits of data presented in Ref. 5. Thermal properties were evaluated at the Eckert reference temperature given by[6]

$$T_r = 0.5T_w + 0.28T_s + 0.22T_{ad} \qquad (11)$$

Reynolds Number

The Reynolds number for all models was based on the diameter, d, of the bare cylinder. For the ice shapes this was 5.1 cm (2.0 in.) and 6.6 cm (2.6 in.) for the cylinder with no ice accumulation. The Reynolds number was calculated as

$$Re = \frac{\rho V d}{\mu} \qquad (12)$$

Nusselt Number

The Nusselt number was also based on the diameter of the bare cylinder with no ice accumulation and was calculated as

$$Nu = \frac{hd}{k} \qquad (13)$$

Data Acquisition and Error Analysis

All data with the exception of the turbulence measurements were recorded on the laboratory data acquisition system which is described in Ref. 7. For each data point, twenty "scans" or individual readings of each data channel were recorded. These twenty scans were then averaged to give a single reading for each channel. This helped to eliminate some of the noise present in the system. Because of the electronic multiplexing of the individual data channels to the analog to digital converter, there is a certain offset between data channels. In an extreme case this caused a 0.6° C indicated difference in thermocouples that were at the same temperature. This was corrected by shorting all the inputs to the data acquisition system after a run, recording this value, then subtracting this "zero" from each reading.

An error analysis was performed for each data point by the method of Kline and McClintock.[8] The average error for all data points was determined to be 5.7 percent and the maximum error was 7.8 percent.

Results and Discussion

In this section, heat transfer distribution in the form of Nusselt number as a function of angle from the stagnation point as well as the variation of Nusselt number with Reynolds number will be presented for the circular cylinder and the four ice accretion shapes. Results will be presented for both smooth and sand roughened shapes for high and low free stream turbulence.

Heat Transfer Distributions

Circular Cylinder

Smooth Surface-Low Turbulence. Figure 9 shows Nusselt number as a function of angle from the stagnation point for the four cases mentioned above. All the data on Fig. 9 was taken at a Reynolds number of 177 000.

Also ploted on the figure is an exact solution of the laminar boundary layer equations due to Frössling.[9] The good agreement between the exact solution and the smooth cylinder, low turbulence data confirms the accuracy of the experimental method.

Smooth Surface-High Turbulence. Nusselt number distribution around the cylinder placed downstream of the bi-plane grid is also shown on Fig. 9. The grid produced turbulence of about 3.5 percent with a scale of 1 cm (0.4 in.). Three and one-half percent turbulence was selected because the IRT was originally thought to be a "dirty" tunnel with about this level of turbulence. Recent hot wire measurements by the authors have shown that in fact the turbulence levels are much closer to 0.5 percent. The effect of turbulence is to increase the heat transfer virtually uniformly around the circumference (measurements were only made up to 50° from stagnation) by about 30 percent.

Rough Surface-Low Turbulence. As seen on Fig. 9, the addition of sand roughness to the cylinder surface does not change the heat transfer rate near the stagnation point from the smooth surface case. As the angle from stagnation increases however, the heat transfer rate also increases. This is most likely due to boundary layer transition.

Rough Surface - High Turbulence. The final set of symbols on Fig. 9 is for the sand roughened surface with 3.5 percent free stream turbulence. The effect of free stream turbulence is seen to be greater nearest the stagnation point where the heat transfer rate is again increased by about 30 percent over the low turbulence case. As the angle from stagnation becomes larger, the effect of free stream turbulence diminishes as the boundary layer becomes more turbulent.

Two Minute Glaze Ice

Figure 10 shows the Nusselt number distribution for a two minute accumulation of glaze ice. The data on this figure was taken at a Reynolds number of 136 000. Also shown on the figure is the exact solution due to Frössling.

Smooth Surface-Low Turbulence. For the smooth surface, low turbulence case, the heat transfer distribution is not changed much from the circular cylinder. There is no gage at the stagnation point but gage number 5 shows that the heat transfer in the stagnation region is only slightly below that for the cylinder. Gages 2, 3, and 4 show only slightly higher heat transfer than the circular cylinder. Gage number 1 is in a region of separated flow and has a somewhat higher heat transfer rate. This region is of relatively low importance because the water drop collection efficiency in this region is near zero and ice does not grow from this location.

4

Rough Surface—Low Turbulence. As with the circular cylinder, the addition of surface roughness drastically changes the heat transfer distribution. The heat transfer in the stagnation region remains nearly the same as for the smooth surface but boundary layer transition causes the heat transfer to nearly triple at gage number 2. The collection efficiency is high in this region and the large heat transfer promotes rapid ice growth.

Rough Surface—High Turbulence. The addition of free stream turbulence increases the heat transfer in the stagnation region. Heat transfer in the region of ice growth is not significantly affected by turbulence however. Turbulence has no effect on heat transfer in the separated region (gage 1).

Five Minute Glaze Ice

The heat transfer distribution for five minutes accumulation of glaze ice is shown on Fig. 11. The exact solution is again shown for reference. Reynolds number for these data was 140 000.

Smooth Surface—Low Turbulence. For this case near the stagnation region (gage 8), the heat transfer is 23 percent lower than for the circular cylinder. As the angle from stagnation increases, the heat transfer increases slightly then decreases to a minimum at gage 6. Heat transfer is a maximum at gage 4.

Rough surface—Low Turbulence. In the stagnation region, heat transfer is the same as the smooth surface case. As with the cylinder, roughness causes the heat transfer to increase dramatically with distance from the stagnation point. The maximum heat transfer rate occurs at gage 4 and is nearly double that of the smooth surface case. It is obvious from examination of the ice shape that the region near gage 4 is the region of fastest ice growth. Roughness does not affect the heat transfer rate in the separated region (gages 1, 2, and 3).

Rough Surface—High Turbulence. Turbulence has the same effect on heat transfer as in the previous examples. Heat transfer is increased in the stagnation region and the increase is not as great in the region of fastest ice growth away from the stagnation region. Turbulence has virtually no effect in the separated region.

Fifteen Minute Glaze Ice

Figure 12 shows the heat transfer distribution for 15-min accumulation of glaze ice. The Reynolds number for all the data on this figure was 136 000. Frössling's exact solution for the cylinder is again plotted for reference.

Smooth Surface—Low Turbulence. Smooth surface results are similar to the previous glaze ice shapes. Heat transfer is lower than for the cylinder near the stagnation region and increases to a maximum at gage 9 which is the location of fastest ice accumulation.

Smooth Surface—High Turbulence. The effect of higher turbulence with the smooth surface is again to increase heat transfer nearly uniformly except in the separated flow region where there is no effect.

Rough Surface—Low Turbulence. Roughness has almost no effect until gage 9 where the heat transfer rate is doubled compared to the smooth surface low turbulence case.

Rough Surface—High Turbulence. Turbulence as in all the other cases, causes a nearly uniform

increase in the heat transfer except in the separated flow region.

Fifteen Minute Rime Ice

Figure 13 shows the heat transfer distribution for 15-min accumulation of rime ice. All data points were taken at a Reynolds number of 138 000.

Smooth Surface—Low Turbulence. Heat transfer levels for the rime ice shape are similar to those for the plane cylinder except near gage 8 where they are slightly higher. It was impractical to locate a gage at the critical region between gages 8 and 9; it is possible that the maximum heat transfer rate occurs at this location.

Smooth Surface—High Turbulence. A nearly uniform increase can be seen in the stagnation region. In the wedge shaped region (gages 1 to 7) there is no effect of turbulence.

Rough Surface—Low Turbulence. The largest increase in heat transfer due to roughness occurs at gage 8. Roughness also increases the heat transfer in the wedge flow region considerably and has less of an effect in the stagnation region. It is possible that roughness causes an even more dramatic increase in the critical region between gages 8 and 9 that cannot be resolved.

Rough Surface—High Turbulence. As in all the previous cases turbulence increases heat transfer in the stagnation region by the largest amount. Heat transfer is increased in other regions by turbulence but to a lesser degree.

Reynolds Number Effects

Data for all models was taken for various flow rates which gave a range of Reynolds numbers from about 50 000 to 180 000. Space limitations prevent us from showing Reynolds number effects for every gage of every model; however, results from gages in critical ice growth areas and ot interesting locations will be shown. For each gage, a least squares fit of the equation

$$Nu = ARe^B \qquad (14)$$

was obtained, the constants A and B for each gage are shown in Table III.

Circular Cylinder

Figure 14 shows Nusselt number as a function of Reynolds number for the gage located at 50° from the stagnation point for the circular cylinder. This is near the location of most rapid ice accumulation. Also shown on the figure is a least squares fit of Eq. (14) for each case. The constants A and B, are shown on the legend of the figure as well as in Table III.

For the smooth surface cases of low and high free stream turbulence, the slope of the curves is seen to be near 0.5 which is indicative of a laminar boundary layer. The addition of surface roughness causes a departure from the power law behavior which is indicative of a transitional boundary layer. In the latter two cases, the least squares fits were computed only for data points with Reynolds numbers greater than 100 000.

Glaze Ice

The effect of Reynolds number on Nusselt number for 2-min accumulation of glaze ice for gage

5

two is shown on Fig. 15. The behavior is similar to that shown previously for the cylinder. The smooth surface case has a 0.5 slope indicating a laminar boundary layer. The addition of surface roughness causes boundary layer transition and a departure from the power law curve fit.

The remaining two glaze ice shapes tested, 5- and 15-min accumulation, show similar trends with Reynolds number and will not be shown here.

Rime Ice

The effect of Reynolds number on heat transfer at gage 9, which is near the location of fastest ice growth, is shown on Fig. 16. The two smooth surface cases have slopes near 0.5 which indicates a laminar boundary layer. The two cases with surface roughness shown an increased slope but, unlike the glaze ice, follow the power law curve fit.

Figure 17 shows the data from gage 4. In this region the ice shape appears wedge-like, i.e., a nearly flat surface at an angle to the free stream. The smooth surface data appears to go thru a rapid transition to a turbulent boundary layer as Reynolds number increases beyond about 70 000. In all cases where this transition takes place, the constants in Table III are valid only for the high Reynolds number portion of the data. The addition of surface roughness or free stream turbulence, however, eliminates this phenomenon.

Summary of Results

Heat transfer measurements have been made on a circular cylinder and on four simulated ice accretion shapes. The ice shapes had a constant cross section perpendicular to the flow and were obtained by averaging cross sections of ice grown on a cylinder in the NASA Lewis Icing Research Tunnel. Heat transfer distributions around the circumference of the ice shapes and circular cylinder were obtained over a range of flow velocities. The effect of surface roughness and free stream turbulence was investigated for each icing shape model. The heat transfer distribution around each model is presented as well as selected Reynolds number effects. Power law curve fits of Nusselt number as a function of Reynolds number are presented in tabular form. Major conclusions were:

1. Surface roughness changes the character of the boundary layer from laminar to transitional. This causes heat transfer to increase in the region of fastest ice growth.
2. Free stream turbulence changes heat transfer most in the stagnation region. The stagnation region is not the region of most rapid ice growth.
3. As glaze ice shapes grow, the difference between heat transfer at the stagnation point and the point of the most rapid growth increases thus promoting even faster growth away from the stagnation region.

References

1. Shaw, R. J., Sotos, R. G., and Solano, F. R.,: "An Experimental Study of Airfoil Icing Characteristics," NASA TM-82790, 1982.
2. Olsen, W. A. J., and Shaw, R. J., "Ice Shapes and the Resulting Aero Penalty for a Typical Helicopter Airfoil," AIAA Paper 84-0109, 1984.
3. Lozowski, E. P., Stallabrass, J. R., and Hearty, P. F., "The Icing of ar Inheated Non-rotating Cylinder in Liquid Water Droplet: Ice Crystal Clouds," National Research Council of Canada, LTR-LT-96, Feb. 1979.
4. Carslaw, H.S., and Jeager, J.C., Conduction of Heat in Solids, 2nd ed., Clarendon Press, Oxford, 1959, p. 167.
5. Hillsenratn, J., Beckett, C. W., Benedict, W. S., Fano, L., and Hobe, H. J., "Tables of Thermal Properties of Gases," NBS Circular 564, Nov. 1955.
6. Eckert, E.R.G., and Drake, R.M., Heat and Mass Transfer, 2nd ed., McGraw-Hill, New York, 1959, p. 270.
7. Miller, R.L., "ESCORT: A Data Acquisition and Display System to Support Research Testing," NASA TM-78909, 1978.
8. Kline, S.J., and McClintock, F.A., "Describing Uncertainties in Single-Sample Experiments," Mechanical Engineering, Vol. 75, Jan. 1953, pp. 3-8.
9. Frössling, N., "Evaporation, Heat Transfer, and Velocity Distribution in Two-Dimensional and Rotationally Symmetrical Laminar Boundary-Layer Flow," NACA TM 1432, 1958.

TABLE I. - ICE SHAPE COORINATES*

Two minute glaze		Five minute glaze		Fifteen minute glaze		Fifteen minute rime	
θ	2r/d	θ	2r/d	θ	2r/d	θ	2r/d
0.43	1.173	0.00	1.314	0.25	1.921	0.00	2.224
7.85	1.187	5.04	1.379	1.72	1.940	1.90	2.257
16.13	1.204	9.42	1.445	3.15	1.971	4.49	2.305
23.03	1.215	11.74	1.461	4.60	1.964	6.26	2.305
30.55	1.231	14.92	1.463	7.31	1.932	8.07	2.267
37.91	1.244	18.27	1.451	10.20	1.885	10.71	2.131
46.62	1.269	22.55	1.439	12.39	1.877	14.46	19.03
51.52	1.264	25.97	1.438	15.03	1.897	22.60	1.532
55.96	1.237	29.78	1.468	18.56	1.951	35.23	1.219
59.50	1.184	33.71	1.532	21.66	2.061	44.65	1.104
61.35	1.148	36.08	1.582	24.03	2.214	53.01	1.042
63.51	1.100	38.60	1.639	25.86	2.343	62.82	1.022
66.11	1.062	41.69	1.704	27.39	2.484	69.96	1.022
69.65	1.032	43.91	1.717	28.94	2.652	75.74	1.034
72.17	1.035	46.03	1.705	30.13	2.818	89.42	1.000
74.66	1.041	47.90	1.660	31.24	2.941		
90.00	1.000	50.14	1.566	32.52	3.003		
		52.43	1.454	34.31	3.039		
		55.76	1.332	35.76	3.031		
		60.93	1.198	37.09	2.984		
		65.97	1.113	37.93	2.893		
		71.21	1.064	38.87	2.766		
		75.12	1.025	43.25	2.229		
		89.43	1.001	53.32	1.566		
				67.42	1.157		
				75.49	1.028		
				90.00	1.000		

*Parameters defined in Fig. 3.

TABLE II. - HEAT FLUX GAGE LOCATIONS*

Two minute glaze		Five minute glaze		Fifteen minute glaze		Fifteen minute rime	
Gage no.	θ	Gage no.	θ	Gage no.	θ	Gage no.	θ
1	62.4	1	67.0	1	64.0	1	65.0
2	45.0	2	57.8	2	57.1	2	51.6
3	33.0	3	52.5	3	52.4	3	40.0
4	19.6	4	46.3	4	48.2	4	31.3
5	7.0	5	36.0	5	45.0	5	24.8
6	-5.4	6	28.0	6	42.8	6	19.4
		7	19.0	7	40.6	7	15.1
		8	5.3	8	38.6	8	11.0
		9	-5.3	9	33.3	9	2.8
				10	29.1	10	-2.5
				11	27.1		
				12	24.4		
				13	20.6		
				14	15.6		
				15	9.5		
				16	2.8		
				17	-2.8		

*Parameters defined in Fig. 3.

TABLE III. - COEFFICIENTS FOR POWER LAW CURVE FIT OF $Nu = ARe^B$ FOR EACH CASE

|	Gage no.	Smooth surface 0.5% turbulence		Rough surface 0.5% turbulence		Smooth surface 3.5% turbulence		Rough surface 3.5% turbulence	
		A	B	A	B	A	B	A	B
Circular cylinder	0°	1.2436	0.4774	0.7636	0.5183	0.6632	0.5533	0.2460	0.6444
	10°	0.9734	0.5008	0.3405	0.6010	0.5287	0.5723	0.1478	0.6920
	20°	0.8373	0.5125	0.0415	0.7941	0.6003	0.5614	0.0306	0.8377
	30°	0.8160	0.5109	0.0094	0.9359	0.6005	0.5583	0.0072	0.9738
	40°	0.6569	0.5241	0.0009	1.1520	0.6076	0.5547	0.0025	1.0778
	50°	0.6460	0.5218	0.0174	0.9137	0.4880	0.5673	0.0469	0.8339
2 minute glaze ice	1	0.0275	0.8056	0.0278	0.8100	———	———	0.0853	0.7237
	2	0.8753	0.5081	0.1221	0.7527	———	———	0.0077	0.9958
	3	1.1081	0.4956	0.0064	0.9945	———	———	0.0086	0.9836
	4	1.2048	0.4887	0.0929	0.7428	———	———	0.0855	0.7703
	5	1.2009	0.4722	0.4326	0.5728	———	———	0.1679	0.6851
	6	1.0173	0.4752	0.5809	0.5308	———	———	0.1418	0.6896
5 minute glaze ice	1	0.1878	0.6531	0.0636	0.7499	———	———	0.1472	0.6824
	2	0.1082	0.6899	0.0424	0.7782	———	———	0.0768	0.7292
	3	0.0525	0.7490	0.0441	0.7710	———	———	0.0681	0.7328
	4	0.4966	0.5613	0.0008	1.1654	———	———	0.0012	1.1424
	5	0.4844	0.5403	0.0036	1.0192	———	———	0.0104	0.9457
	6	0.8144	0.4686	0.0084	0.9038	———	———	0.0149	0.8842
	7	1.0663	0.4734	0.1469	0.6544	———	———	0.0403	0.7992
	8	0.4734	0.5289	0.3364	0.5592	———	———	0.2831	0.6174
	9	0.6399	0.4998	0.4072	0.5400	———	———	0.2197	0.6378
15 minute glaze ice	1	0.0915	0.7364	0.0163	0.9081	0.1177	0.7142	0.0283	0.8596
	2	0.0757	0.7400	0.0124	0.9195	0.0950	0.7187	0.0194	0.8794
	3	0.0500	0.7663	0.0145	0.8941	0.0593	0.7499	0.0194	0.8664
	4	0.0495	0.7658	0.0156	0.8804	0.0621	0.7447	0.0236	0.8431
	5	0.0358	0.7854	0.0187	0.8526	0.0474	0.7594	0.0242	0.8289
	6	0.0340	0.7829	0.0204	0.8338	0.0488	0.7504	0.0263	0.8104
	7	0.0327	0.7827	0.0153	0.8575	0.0421	0.7588	0.0209	0.8285
	8	0.0281	0.7979	0.0139	0.8735	0.0432	0.7595	0.0213	0.8337
	9	1.1024	0.5387	0.0059	1.0452	0.8322	0.5819	0.0121	1.0021
	10	0.5132	0.5207	0.0347	0.7798	0.3698	0.5885	0.0421	0.8029
	11	0.4821	0.5105	0.1026	0.6575	0.2487	0.6121	0.0495	0.7713
	12	0.3085	0.5344	0.1224	0.6208	0.2058	0.6196	0.0463	0.7633
	13	0.3219	0.5208	0.1562	0.5857	0.2205	0.6077	0.0444	0.7598
	14	0.2922	0.5254	0.1522	0.5847	0.1829	0.6179	0.0356	0.7755
	15	0.1206	0.6073	0.0647	0.6644	0.1211	0.6502	0.0288	0.8005
	16	0.1259	0.6215	0.0632	0.6828	0.1761	0.6474	0.0511	0.7699
	17	0.1265	0.6166	0.0810	0.6609	0.2134	0.6260	0.0541	0.7658
15 minute rime ice	1	0.3093	0.6136	0.0231	0.8781	0.0613	0.7549	0.0201	0.8973
	2	0.1543	0.6733	0.0493	0.8015	0.0267	0.8256	0.0352	0.8395
	3	0.0313	0.7999	0.0384	0.8151	0.0089	0.9078	0.0265	0.8571
	4	0.0352	0.7958	0.0356	0.8256	0.0187	0.8491	0.0197	0.8863
	5	———	———	0.0509	0.7993	0.0126	0.8895	0.0367	0.8371
	6	———	———	0.0888	0.7546	0.0095	0.9125	0.0494	0.8138
	7	———	———	0.0807	0.7772	0.0405	0.7858	0.0645	0.8035
	8	0.0043	0.9844	0.0048	1.0468	0.0785	0.7653	0.0408	0.8750
	9	1.0146	0.5030	0.2548	0.6447	0.6615	0.5726	0.1569	0.7187
	10	1.2511	0.4831	0.8081	0.5342	0.6449	0.5740	0.1953	0.6898
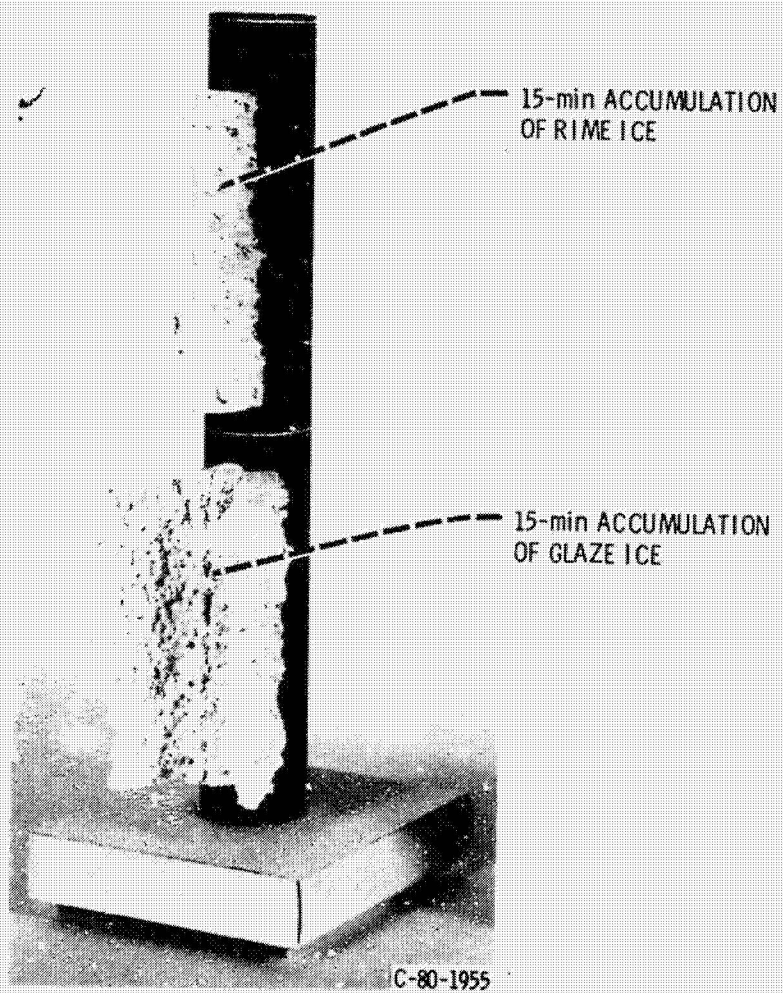
Figure 1. - Plaster casts of 15-min accumulation of both rime and glaze ice on a 5.1 cm (2.0 in.) diameter cylinder.
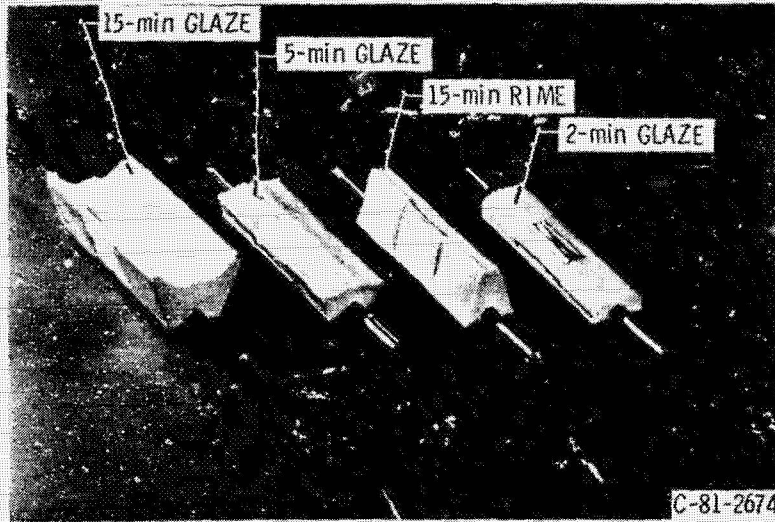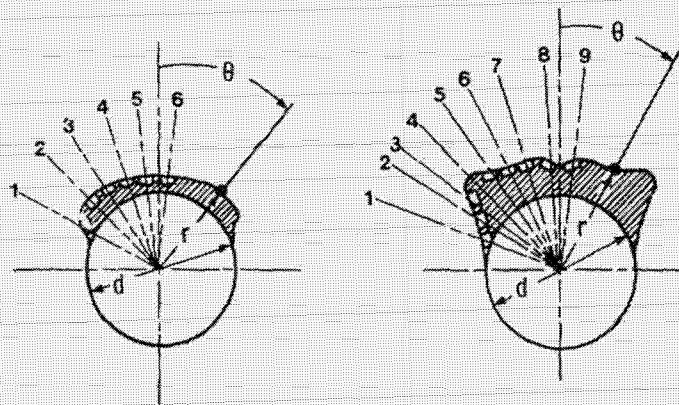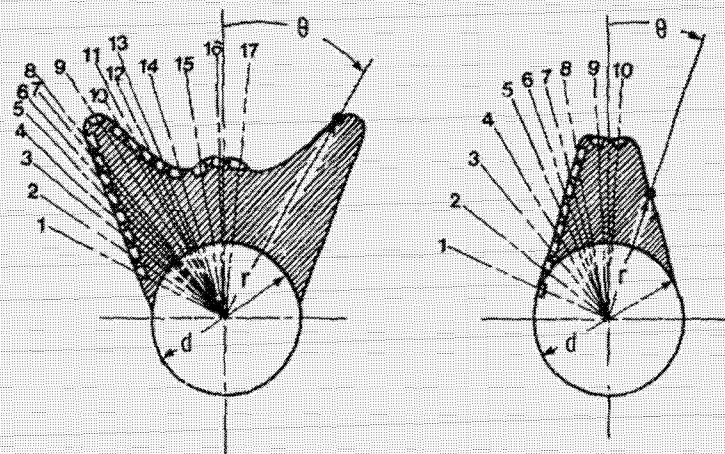
Figure 2. - Photograph of icing shape heat transfer models.

(a) Two minute glaze ice.

(b) Five minute glaze ice.

(c) Fifteen minute glaze ice.

(d) Fifteen minute rime ice.

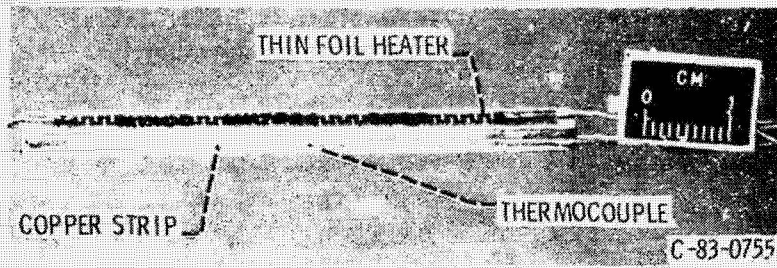Figure 3. - Ice shape cross sections showing profile coordinates and heat flux gage locations.
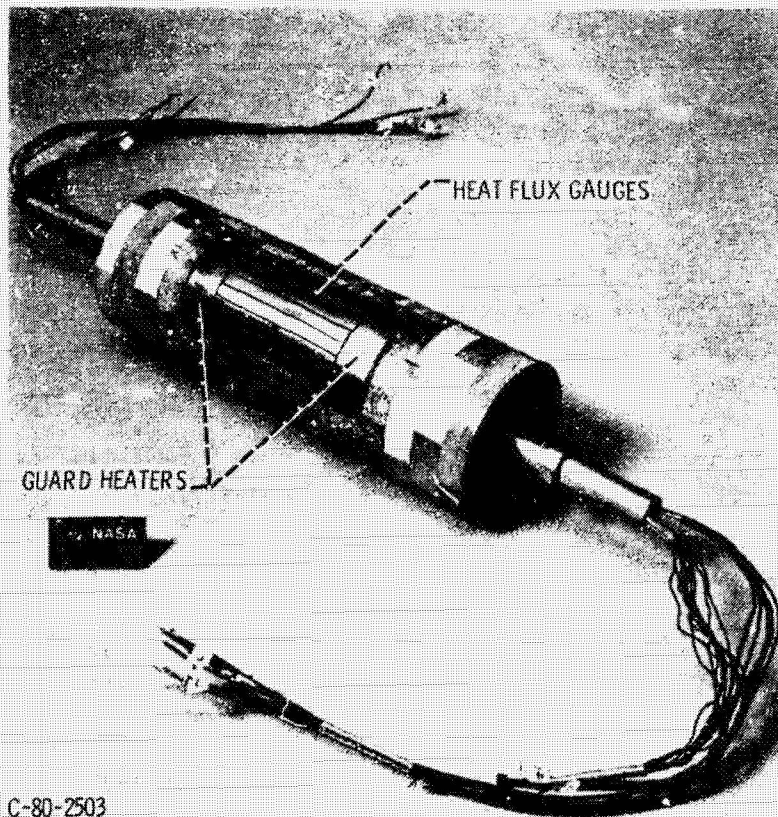
Figure 4. - Photograph of heat flux guage.

Figure 5. - Cylinder heat transfer model.
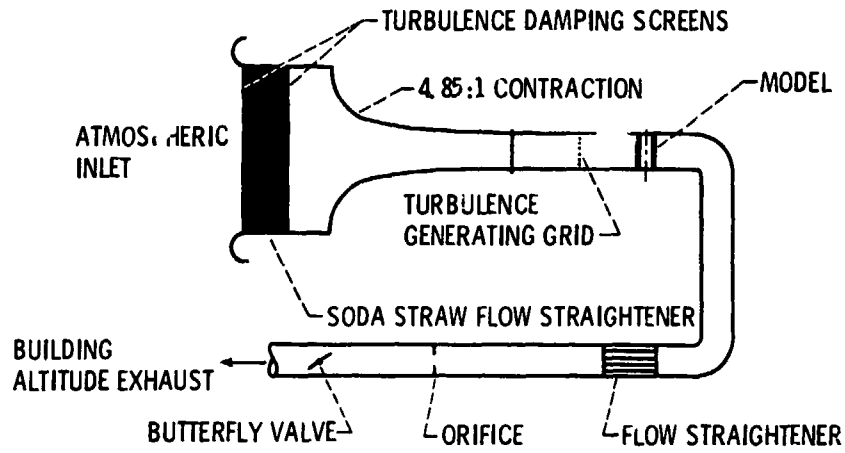
Figure 6. - Wind tunnel schematic.
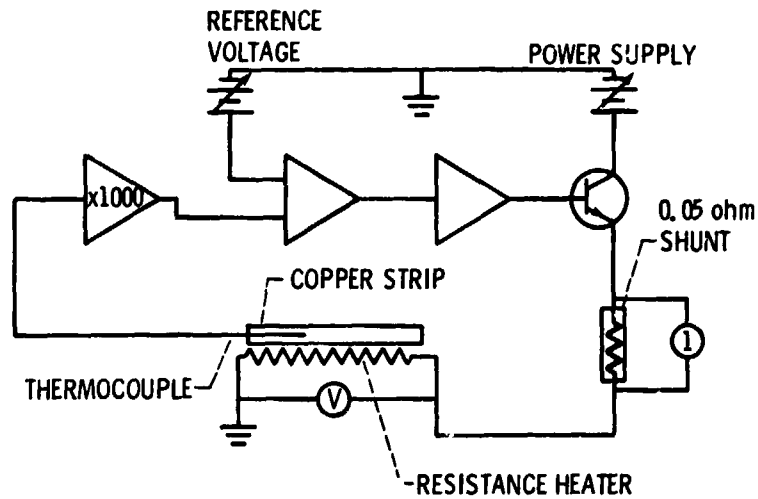
Figure 7. - Schematic of automatic heat flux gage temperature controller.

Figure 9. – Heat transfer distribution for circular cylinder.
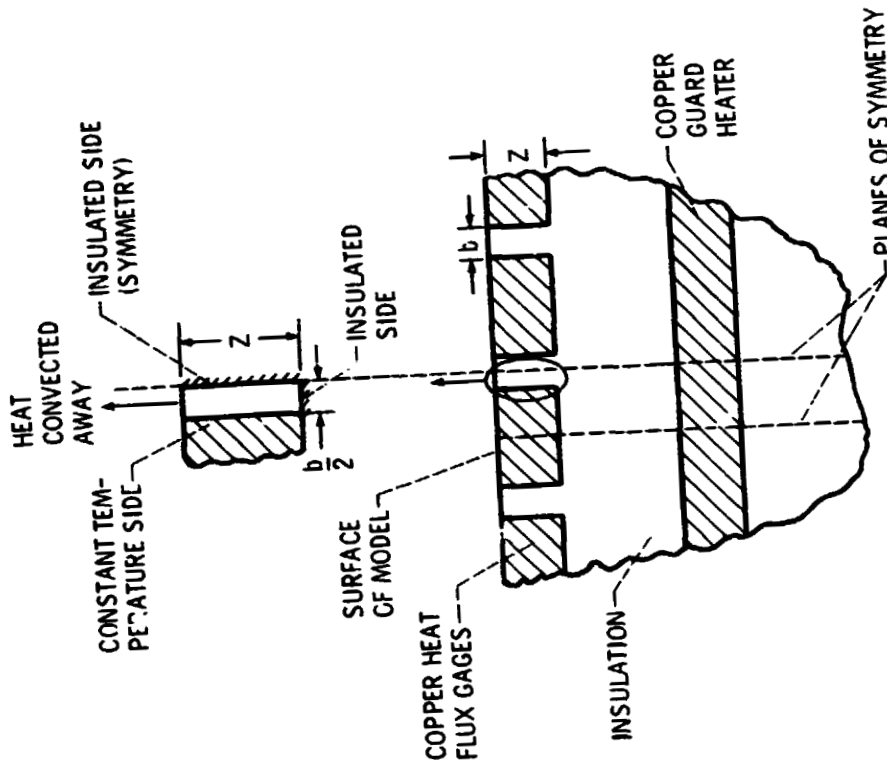
Figure 8. – Insulation gap heat loss model.

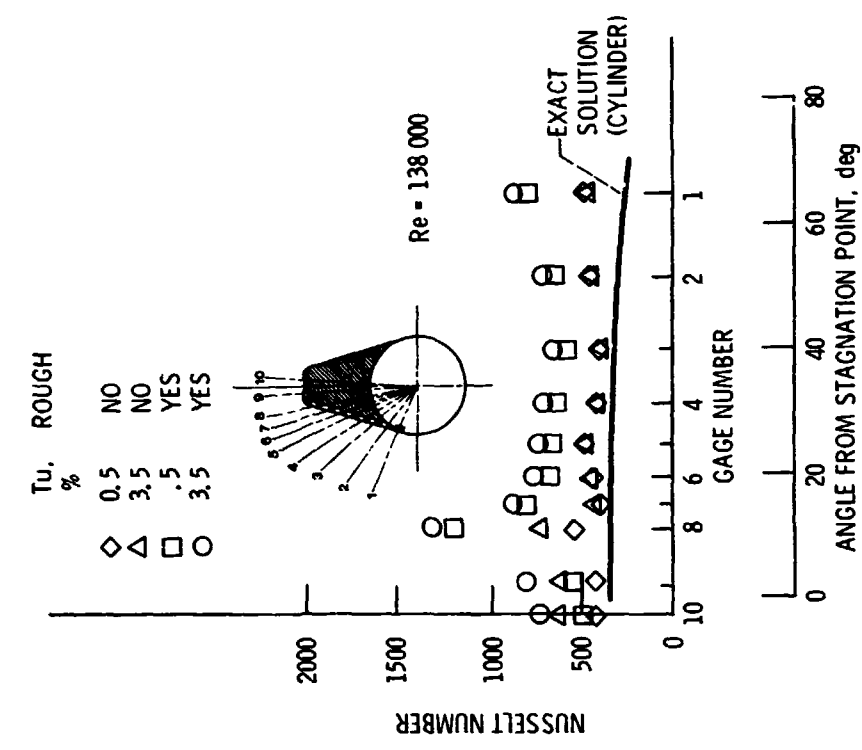Figure 11. – Heat transfer distribution for five minutes accumulation of glaze ice.

Figure 10. – Heat transfer distribution for two minutes accumulation of glaze ice.

Figure 13. – Heat transfer distribution for fifteen minutes accumulation of rime ice.

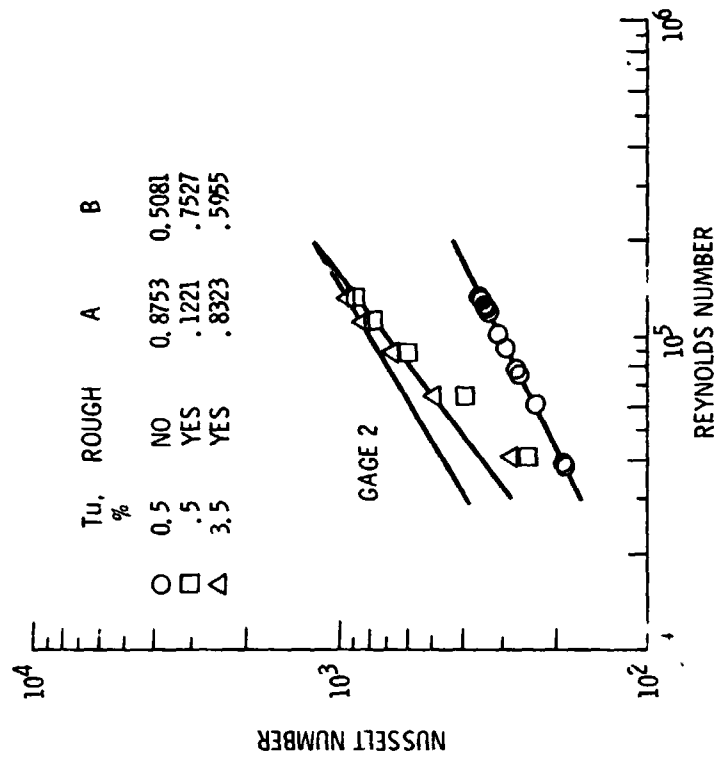Figure 12 – Heat transfer distribution for fifteen minutes accumulation of glaze ice.

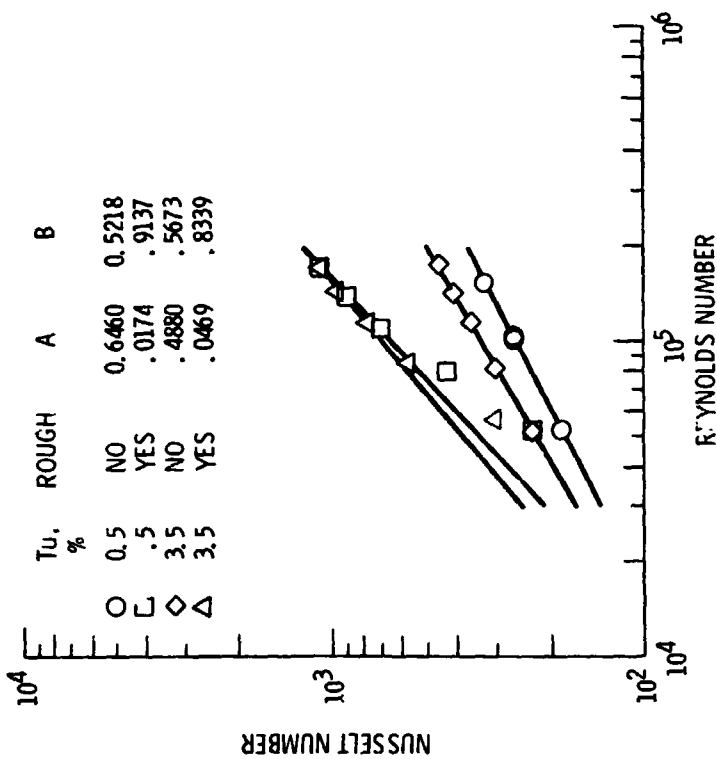Figure 15. – The effect of Reynolds number on heat transfer for two minutes accumulation of glaze ice at gage 2.

Tu, %	ROUGH	A	B
0.5	NO	0.8753	0.5081
.5	YES	.1221	.7527
3.5	YES	.8323	.5955

GAGE 2

Figure 16 – The effect of Reynolds number on Nusselt number for the circular cylinder at θ = 50°.

Tu, %	ROUGH	A	B
0.5	NO	0.6460	0.5218
.5	YES	.0174	.9137
3.5	NO	.4880	.5673
3.5	YES	.0469	.8339

GAGE 4

NUSSELT NUMBER

REYNOLDS NUMBER

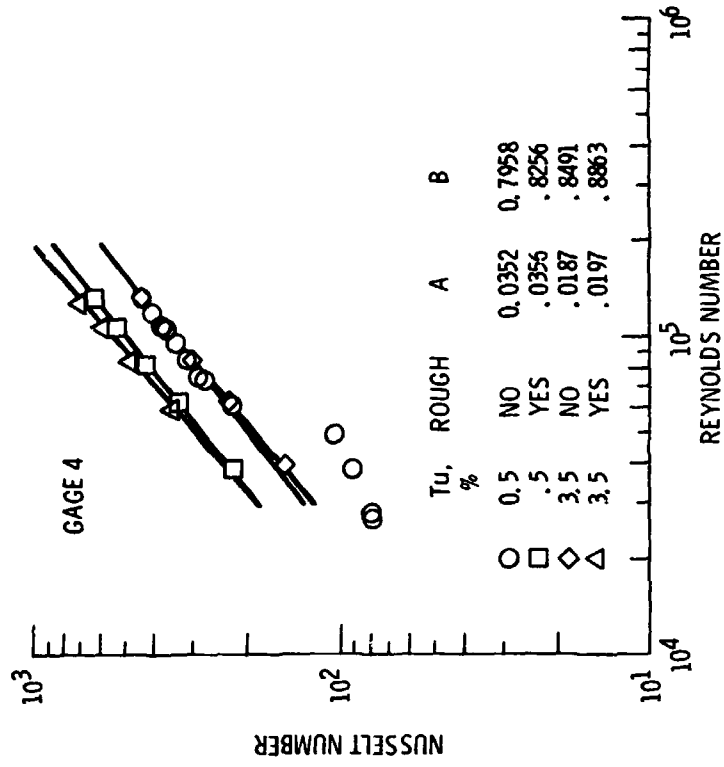| Tu, %	ROUGH	A	B
◯ 0.5	NO	0.0352	0.7958
▢ .5	YES	.0356	.8256
◇ 3.5	NO	.0187	.8491
△ 3.5	YES	.0197	.8863

Figure 17. – The effect of Reynolds number on heat transfer
for fifteen minutes accumulation of rime ice at gage 4.

GAGE 9

NUSSELT NUMBER

REYNOLDS NUMBER

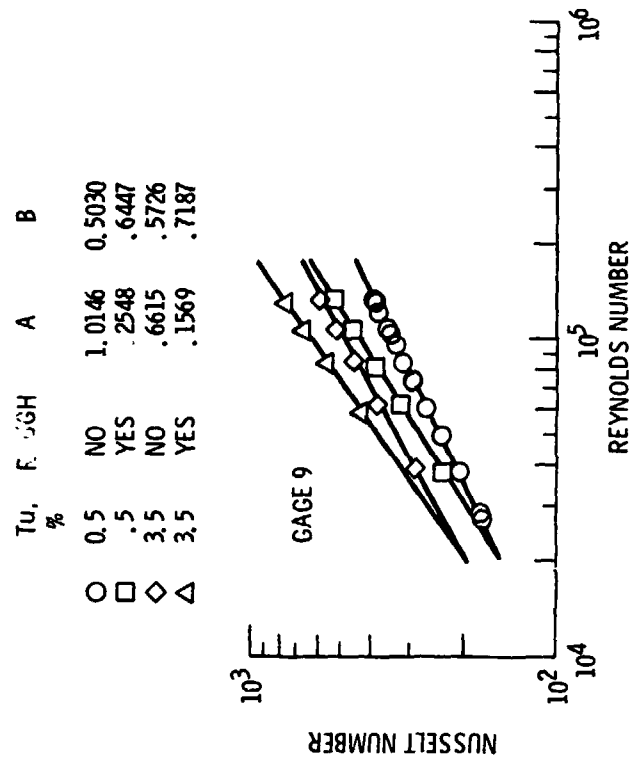| Tu, %	ROUGH	A	B
◯ 0.5	NO	1.0146	0.5030
▢ .5	YES	.2548	.6447
◇ 3.5	NO	.6615	.5726
△ 3.5	YES	.1569	.7187

Figure 16. – The effect of Reynolds number on heat transfer
for fifteen minutes accumulation of rime ice at gage 9.